Journal of Electron Spectroscopy and Related Phenomena 170 (2009) 25–36

Contents lists available at ScienceDirect

Journal of Electron Spectroscopy and Related Phenomena

journal homepage: www.elsevier.com/locate/elspec

Radiation damage in soft X-ray microscopy

J. Wang[a], C. Morin[a], L. Li[a], A.P. Hitchcock[a,*], A. Scholl[b], A. Doran[b]

[a] Department of Chemistry and Brockhouse Institute for Materials Research, McMaster University, Hamilton, ON, Canada L8S 4M1
[b] Advanced Light Source, Berkeley Lab, Berkeley, CA 94720, United States

ARTICLE INFO

Article history:
Available online 4 May 2008

Keywords:
Radiation damage
Soft X-rays
Photoemission electron microscopy
Scanning transmission X-ray microscopy
Polystyrene
Poly(methyl methacrylate)
Fibrinogen
Polymer thin films

ABSTRACT

The rates of chemical transformation by radiation damage of polystyrene (PS), poly(methyl methacrylate) (PMMA), and fibrinogen (Fg) in a X-ray photoemission electron microscope (X-PEEM) and in a scanning transmission X-ray microscope (STXM) have been measured quantitatively using synchrotron radiation. As part of the method of dose evaluation in X-PEEM, the characteristic (1/e) sampling depth of X-PEEM for polystyrene in the C 1s region was measured to be 4 ± 1 nm. Critical doses for chemical change as monitored by changes in the X-ray absorption spectra are 80 (12), 280 (40) and 1230 (180) MGy (1 MGy = 6.242*ρ eV/nm^3, where ρ is the polymer density in g/cm^3) at 300 eV photon energy for PMMA, Fg and PS, respectively. The critical dose for each material is comparable in X-PEEM and STXM and the values cited are thus the mean of the values determined by X-PEEM and STXM. C 1s, N 1s and O 1s spectroscopy of the damaged materials is used to gain insight into the chemical changes that soft X-rays induce in these materials.

1. Introduction

Radiation damage occurs whenever ionizing radiation is absorbed by a material. In biological materials – proteins, nucleic acids, cells and multi-cell organisms – very low doses (a few Gray) are sufficient to modify and inactivate biomacromolecules, and thus incapacitate or kill organisms [1,2], while somewhat higher doses impede structural studies by crystallography, unless the crystal is cooled [3]. In inanimate materials changes caused by radiation include formation of defects in ionic and semiconductor materials [4], and changes in covalent bonding, and ultimately mass loss via elimination of low molecular weight fragments in organic materials [5]. In this work we are concerned with characterizing the nature and rate of chemical changes caused by soft X-rays in modern synchrotron soft X-ray microscopes, specifically in the techniques of X-ray photoemission electron microscopy (X-PEEM) [6–9] and scanning transmission X-ray microscopy (STXM) [10–15]. Both techniques are mostly carried out using high brilliance third generation synchrotron facilities which provide high dose rates which can lead to damage, particularly in soft materials such as polymers and biological samples. These microscopies are being used successfully to study a wide range of scientific problems, ranging from environmental biofilms [16], water filtration membranes [17], polymer microspheres and capsules for chemical [18] and pharmaceutical delivery [19], fundamental polymer physics [20], biomaterials [21–23], among many other areas. In both X-ray microscopies, radiation damage limits the precision in some cases [14,17,22,24–30], even when cryo-techniques [25,26,31] are used. Cryo-techniques are effective in minimizing mass loss; however damage to chemical bonds has been found to occur at the same rate as at room temperature [32]. This work deals with soft X-ray damage at room temperature, where most materials studies are carried out. In our previous studies of fibrinogen adsorption on a phase segregated surface of a polystyrene/polymethyl-methacrylate blend, radiation damage to polymethylmethacrylate leads to a signal that could be mistaken for either polystyrene [20] or fibrinogen [22]. Brandes et al. [27] used STXM to analyze carbohydrates in the marine sinking particulate organic matter (POM). Radiation damage occurred as a decrease in the dominant 289.5 eV feature, and an increase in a new peak at 286.5 eV. Although a number of ways were tried to minimize this problem, the radiation damage effect still could not be eliminated. Biological samples are rather susceptible to radiation damage. For example, Anderson et al. [28] used air-dried melanosomes for X-ray microscopic analysis, which experienced significant damage during spectral scans, often abruptly rupturing. This problem was fortunately solved by utilizing a freeze-drying protocol. Thus, it is essential to characterize both the rate and the nature of the spectroscopic changes that accompany radiation damage, in order to identify damage when it occurs and to be able to select acquisition strategies that give maximum amount of mean-

* Corresponding author at: Brockhouse Institute for Materials Research, McMaster University, 1280 Main Street West, Hamilton, ON, Canada L8S 4M1.
Tel.: +1 905 525 9140x24749; fax: +1 905 521 2773.
E-mail address: aph@mcmaster.ca (A.P. Hitchcock).

0368-2048/$ – see front matter © 2008 Elsevier B.V. All rights reserved.
doi:10.1016/j.elspec.2008.01.002

ingful information for a given level of damage. An aspect of this issue is cross-comparison of X-PEEM and STXM with regard to their relative sensitivity per unit damage for a given analytical problem.

Soft X-ray damage rates in polymers and biological materials have been measured previously, both through near edge X-ray absorption spectroscopy [33,34] and spectromicroscopy [32,35,36]. More generally there is an extensive literature on the chemical effects of high energy electrons, hard X-rays and gamma rays [2,37,38], especially in microscopes [39,40] where radiation doses are typically high. With regard to the relative impact of radiation damage on chemical analysis, Rightor et al. [33] compared the damage rates of poly(ethylene terephthalate) by soft X-rays and 100 keV electrons as measured by X-ray absorption and electron energy loss spectroscopy. As deduced from the changes in the near edge spectra, the damage products were the same in the two cases. This is as expected since much of the damage in each technique arises from secondary electrons rather than the primary absorption or inelastic scattering events. Interestingly, when the photon and electron damage rates were compared in terms of equivalent information, that study found a ~500-fold advantage in terms of analytical information per unit damage for X-ray absorption relative to electron energy loss in a TEM [33]. Jacobsen's group has made several quantitative studies of radiation damage in the Stony Brook STXM at NSLS, including quantitative studies of the damage rate for PMMA at room and liquid nitrogen temperatures and at both the C 1s [35] and O 1s [32] edges. Coffey et al. [36] used C 1s near edge X-ray absorption spectroscopy (NEXAFS) spectroscopy also recorded in the Stony Brook STXM to study radiation chemistry of a series of common polymers that contain the carbonyl functional group. Both groups used a first-order kinetics model to characterize radiation damage in terms of a critical dose parameter, which is the dose required to attenuate the intensity of a specific spectroscopic feature by $(1 - e^{-1})$ or 63%. Coffey et al. [36], emphasized the need to control the local environment in quantitative dose–damage studies as the damage rates and damage chemistry differ significantly between a He and an air environment.

This work is an investigation of the quantitative dose–damage relationship for polystyrene (PS), polymethylmethacrylate (PMMA), and protein (fibrinogen (Fg)), using two different X-ray microscopies, X-PEEM and STXM. Characteristic critical doses for each material are derived following irradiation at several different photon energies (specifically, PMMA and Fg at 300 eV in STXM, PS at 285.1 eV in STXM and PMMA, PS and Fg at each core edge in X-PEEM). The relative damage rates in X-PEEM and STXM are compared. The damage chemistry has been studied by comparing the C 1s, N 1s and O1s NEXAFS spectra of the damaged and undamaged materials. Based on these quantitative dose–damage measurements, procedures in X-PEEM and STXM are recommended which allow analysis of these materials with damage restricted to a level that has minimum impact on chemical analysis. We also suggest general procedures for deriving dose limits for X-ray microscopy studies of other materials.

To our knowledge, NEXAFS studies of the dose/damage relationship of protein have not been reported, although the effect of X-ray damage on the structure of protein crystals has been investigated [2,41]. A study investigating the effects of radiation damage on fluorescent yield NEXAFS and XPS spectra of amino acids was reported recently [34], but critical doses were not determined. There is an extensive literature on damage rates of organic materials by X-ray photoelectron spectroscopy [42].

This paper is organized as follows. Section 2 outlines materials, experimental methods, and the approaches used to interpret the results. Section 3 presents the dose–damage results from X-PEEM and STXM for all three materials. Critical doses are derived and compared to literature values. Section 4 presents the spectroscopy of the radiation damage and discusses the likely chemical transformations that are occurring. Section 5 recommends procedures for minimizing the impact of radiation damage in soft X-ray microscopy.

2. Experimental

2.1. Sample preparation

2.1.1. PMMA and PS

PMMA (MW = 312 K, polydispersity index $\delta = 1.01$) and PS (MW = 1.07 M, $\delta = 1.06$) were obtained from Polymer Source Inc. and used without further purification. A 1 wt% toluene solution was prepared using anhydrous toluene (Aldrich, 99.8%). For X-PEEM sample preparation, a 50 μl drop was spun cast (4000 rpm, 30 s) onto clean, 1 cm^2, native oxide Si wafers (1 1 1) (Wafer World, Inc.), which had previously been degreased with trichloroethylene (Aldrich, +99.5% pure), acetone (Burdick & Jackson, HPLC grade), and methanol (Caledon), then rinsed under running milli-Q water. In order to make uniform films to determine the X-PEEM sampling depth, the PS thin films on Si substrates were further annealed at 140 °C for 4 h in a vacuum oven with pressure $<10^{-2}$ torr achieved by a liquid nitrogen trapped rotary pump or a turbo pump. Then the X-PEEM sampling depth was measured by recording the signal from PS films of varying thickness which were prepared on clean, native oxide silicon using the same spin coating procedure. Non-contact mode atomic force microscopy (AFM) (Veeco Digitial Instruments Nanoscope III or Quesant Q-scope 350) instruments was used to characterize the polymer films. A sharp tweezer tip was used to scratch through the polymer film and the profile across the scratch was measured by AFM to determine the film thickness. PS films made by spin coating (4000 rpm) of toluene solutions of concentrations of 0.05, 0.1, 0.5, 1 and 2 wt% had measured thicknesses of 2, 5, 16, 32, and 95 nm, respectively.

The STXM sample was prepared from the same solution and spun cast onto silicon nitride (Si_3N_4) windows (750 μm × 750 μm window back etched into a 7.5 mm × 7.5 mm × 200 μm silicon wafer chip coated with 75 nm of Si_3N_4), which were obtained from Silson Ltd. [43] and were rigorously cleaned to semiconductor industry standards by the manufacturer. They were stored in gelatin capsules and used without further surface preparation. The thickness of the polymer films was non-uniform due to sagging of the Si_3N_4 membrane while spinning. However, it was possible to find uniform regions larger than 10 μm × 10 μm which were suitable for quantitative radiation damage studies with STXM. For PMMA, large uniform free standing films were also prepared by spin coating (3000 rpm, 30 s) onto a freshly peeled mica surface of 2.5 cm × 2.5 cm. The film was dried in ambient at room temperature, then was cut into 3 mm × 3 mm pieces on the mica surface, and was subsequently floated onto milli-Q water. Two or 3 film pieces were transferred to a degreased hexacomb grid or a TEM grid for STXM experiments. The single layer film thickness was ~40 nm according to STXM measurements.

2.1.2. Protein samples for X-PEEM and STXM

Plasminogen-free human plasma fibrinogen (Calbiochem) was used as received. It is reported to be >95% clottable by thrombin, and pure as judged by sodium dodecyl sulphate polyacrylamide gel electrophoresis. The X-PEEM sample was prepared by spin casting 50 μl of a 1.0 mg/ml Fg solution in deionized water (4000 rpm, 30 s) onto clean, 1 cm^2, Si wafers (same origin and cleaning protocol as above). The STXM sample was prepared by solvent casting, i.e. depositing a 50 μl drop of the same solution onto a clean Si_3N_4 window, without spin coating.

2.1.3. HF-etched Si – X-PEEM I_0 substrate

The substrates used to measure the incident flux (I_0) in X-PEEM were Si wafer chips cleaned as described in Section 2.1.1. Just prior to use they were exposed for 30 s to 10% HF (Aldrich, 48 wt% in water, 99.99+%), then rinsed under running deionized water. The HF-etched Si was mounted on the same sample holder, next to the sample of interest and brought under vacuum within 10 min of preparation. No O 1s signal was detected.

2.2. X-PEEM

The PEEM2 instrument at beamline 7.3.1 of the Advanced Light Source (ALS) was used. Details of the instrument [8] and the operating principles [20] have been presented elsewhere. In order to quantify the dose received by the sample, it is necessary to know the spot size on the sample, the incident flux, the sampling depth and thus the absorbed dose, and the fraction of that absorbed dose contributing to the detected signal. A pseudo exit slit vertically limits the size of the X-ray beam on the sample through two different slit sizes, i.e. 50 and 100 μm. With the pseudo exit slit installed, the sample is not illuminated uniformly due to edge diffraction effects. To circumvent this problem, we only measure the regions over which illumination is relatively uniform. In order to remove higher order light, a Ti filter (200 nm, Lebow) was used for the C 1s and N 1s measurements, but it was removed for the O 1s measurements. The duty cycle of X-PEEM acquisition was also optimized in order to limit un-necessary damage: first a shutter is used so that X-rays impinge on the sample only during measurements; second data binning operations can be directly applied during data acquisition to reduce data transfer times. All X-PEEM data acquired were scaled to 400 mA ring current to compensate for the actual ring current during any given measurement. The data used in determining the critical dose were recorded by repetitively acquiring X-PEEM spectra on the same damage region. After a specific exposure time on the sample at a fixed photon energy or a range of photon energies, the NEXAFS spectrum of the damaged region was acquired using a short image sequence (stack) to evaluate the damage in terms of peak area change. The spectra were derived by averaging the signal at all pixels in the damaged region or from specific sub-regions, if the damage region was not uniform. Flat-field and dark current corrections were directly applied during data acquisition. After measuring the sample, the sample puck was translated to place the I_0 substrate, an HF-etched Si wafer, under the objective lens of the X-PEEM without changing the height of the sample so as to maintain the same energy scale and illumination. The incident flux (I_0 spectrum) was recorded and calibrated with a silicon photodiode [44] according to the details presented in the Supplemental Material. The absolute dose and dose rate in the X-PEEM was derived from incident flux measurements and the sampling depth. The absorbed dose (in units of mega grays, where 1 MGy = 10^6 J/kg (1 MGy = 6.242*ρ eV/nm^3, where ρ is the polymer density in g/cm^3) was obtained as:

$$a = \frac{F \times E \times t}{m} \quad (1)$$

where F is the absorbed flux (photons per second absorbed into the volume contributing to the measured signal), E is the photon energy, t is the exposure time, and m is the mass of the volume. Since the Beer-Lambert law is obeyed for soft X-ray spectromicroscopy applied to thin samples, the absorbed flux can be derived from the incident flux (I_0) and the optical density (absorbance) of the material at the energy of exposure. The optical density (OD) of the sample can be further considered as a product of the linear absorption coefficient (A, optical density per nm, in nm^{-1}) of the material and the sampling depth (d, in nm).

$$F = I_0 - I = I_0 \times (1 - e^{-OD}) = I_0 \times (1 - e^{-A*d}) \quad (2)$$

In order to determine the critical dose for damage of a specific material from the measured damage-exposure data, the damage versus dose data was fit to postulated rate laws, such as a first-order kinetic process [32,33,35,36] which appears to be suitable in cases where mass loss is relatively small and the damage is mainly chemical change. Specifically, the critical dose for damage in X-PEEM was determined by plotting the area of the C 1s → $\pi^*_{C=O}$ and C 1s → $\pi^*_{C=C}$ peaks (or the change of peak area) as a function of radiation dose a. Then the critical dose for the sample material was derived from the dose–damage data by mathematical fitting it with [32,33,35,36]:

$$D = D_\infty + A \exp\left(-\frac{a}{a_c}\right) \quad (3)$$

where D is a relative measure of damage, D_∞ is the saturation damage in the same scale, A is a constant, which has similar magnitude as D_∞ if mass loss is small or negligible in most of our cases, (otherwise a large difference between A and D_∞ indicates that significant mass loss occurs), a is radiation dose, and a_c is the critical dose, which is the dose that attenuates (or increments) a specific spectroscopic feature by 63%. Thus, if the damage process follows first-order kinetics, a plot of $\ln(D - D_\infty)$ versus dose a (in MGy) should be linear with a slope of $-1/a_c$. In some cases, when the dose–peak area profile was far from the damage saturation, the saturation level (D_∞) was estimated based on extrapolation using this functional form.

2.3. STXM

Scanning Transmission X-ray Microscopy (STXM) was performed using the polymer STXM [15] at beamline 5.3.2 [45] at the Advanced Light Source. STXM uses a Fresnel zone plate to focus monochromated X-rays to a small probe. With the zone plates used in this work (diameter of 155 μm, 35 nm outer zone size [46]), the diameter of the beam at focus is ~40 nm, as judged by evaluation of the diffraction limited spatial resolution. The sample is raster scanned with synchronized detection of transmitted X-rays to measure the energy dependent absorption by a column of material. In order to investigate radiation damage rates, adjacent small regions of the sample (typically 0.6 μm × 0.6 μm, using 10 × 10 pixels) were exposed using systematically varied dwell times so as to span a range of doses that adequately sample the dose–damage curve. The entrance and exit slits were adjusted to control the photon flux and dose rate on the sample. Since the point size changes slightly with changes in the slit sizes, the dose was evaluated by considering the flux passing through the uniform central portion of the damage pads (~60%), from which signals at single energies or spectra were extracted. The damaged region was analyzed by imaging it at the photon energy giving the best contrast of the damaged relative to the undamaged material, which was at the strong C 1s → π* transitions (285.15(5) eV for PS, 288.45(5) eV for PMMA and 288.20(5) eV for Fg). The NEXAFS spectra of the damaged and undamaged regions were acquired using an image sequence (stack [47]) with much lower photon flux achieved by reduced slit settings. Reference spectra on absolute linear absorbance scales (i.e. OD per nm thickness of sample) were derived by scaling the spectra of the undamaged material to the X-ray absorption response in the regions of 275–282 eV and 320–350 eV, to match that of the linear X-ray absorption for the elemental composition of the sample derived from literature absorption coefficients [48].

The dose in STXM was also obtained using Eqs. (1) and (2) with the known optical density of the sample, the incident flux, the

irradiated sample area (central 60% of the pad), the sample thickness (d, also the sampling depth in STXM), which is easily derived from the measured optical density and the linear absorption coefficient, and the sample density ρ (see the example for PMMA in the Supplemental Material). The incident flux was measured in a region without the sample (through a hole, or bare part of the silicon nitride window, as appropriate). The measured flux was corrected for the detector efficiency (ε), which was further calibrated to be $35 \pm 5\%$ in the C 1s region by silicon photodiode. A N_2 gas filter (1 m path length at ~1 torr) was used to ensure that the incident photon beam contained negligible higher order radiation. This can be quite important in quantitative dose–damage studies for polymers containing nitrogen or oxygen since the second order photon flux is quite large in beamline 5.3.2 (without the N_2 gas filter), and these second order photons deposit twice the amount of energy per absorbed photon. Similar to X-PEEM, the critical dose for damage in STXM was determined from the damage, expressed in terms of change in signal, usually optical density, at a damage-sensitive energy, as a function of radiation dose by fitting with Eq. (3).

3. Quantitative dose–damage results

3.1. X-PEEM sampling depth

In order to determine the sampling depth, C 1s spectra were measured for a series of thin films of polystyrene with thicknesses of 2, 5, 16 and 32 nm, as measured using AFM to profile a scratch (uncertainty in film thickness from the AFM is <1 nm). Fig. 1 plots the signal at 285.1 eV (C 1s → π* transition of PS) and at 282 eV (where the signal from the underlying silicon substrate is intrinsically stronger) as a function of the film thickness. The inset to Fig. 1 shows the measured spectra, which have been normalized to the signal in the adjacent scratch (that from Si). These measurements indicate that almost all of the signal arises from the outer 10 nm, although there are still small contributions from layers as deep as 20 nm. We have used 10 nm as the total sampling depth in evaluating the absorbed dose, and in deriving quantitative amounts in studies of protein adsorption on PS/PMMA blends [23]. However, since both the absorbed energy and the amount of material vary linearly with sampling depth (since very little of the incident X-ray flux is absorbed in the sampling depth), this factor cancels in determining the critical dose (the thickness enters linearly in determining both the amount of energy absorbed and the mass of material).

The variation of signal with the PS film thickness has been fit to an exponential which yields a characteristic sampling depth (1/e decrease from the maximum detected C 1s signal or increase in the detected Si signal) of 4 ± 1 nm for X-PEEM of polystyrene in the C 1s region. This measured value of 4 nm for PS is in good agreement with a value of 3.5 nm for the escape depth of carbon KLL Auger electrons in multilayers of n-alkanes reported by Zharnikov et al. [49]. It is also similar to values of 3 nm (for 120 eV photon energy) and 5 nm (for 460 eV photon energy) reported by Frazer et al [50] for the X-PEEM sampling depth in Cr metal. For the latter situation, this level of agreement is rather surprising since metals have much greater density of states for low energy electrons and Cr is about seven times denser than polymers, thus Cr would be expected to scatter the slow electrons that dominate X-PEEM signals to a much greater extent. At the same time metals have much lower work functions, which will enhance yield. There could be a fortuitous cancellation of effects at work, since the sampling depth is a complex function of near surface electron transport, and work function, which differ considerably between polystyrene and chromium.

3.2. PMMA – radiation damage in X-PEEM

Fig. 2 presents a series of time- and thus dose-dependent spectra, acquired by successive X-PEEM measurements from the same area of a ~60 nm thick PMMA film on a Si substrate. Each spectrum was normalized to the ring current and the shape of the I_0 signal (which in turn was corrected for the photoabsorption cross section for Si and the bolometry effect for electron yield) [23]. The absolute dose was derived as outlined above. As the accumulated dose increases, the intensity of the C 1s (C═O) → $\pi^*_{C=O}$ transition at 288.4 eV decreases. Simultaneously a peak grows in at 285.1 eV, corresponding to the C 1s (C═C) → $\pi^*_{C=C}$ transition of re-arranged and reduced parts of the polymer backbone.

Fig. 3 presents spectra and dose–damage curves for radiation damage by irradiating PMMA at 300 eV in the X-PEEM. The inset to Fig. 3a is an image of PMMA under the low-magnification conditions used for the damage study, along with boxes identifying the different regions of PMMA that were measured in order to

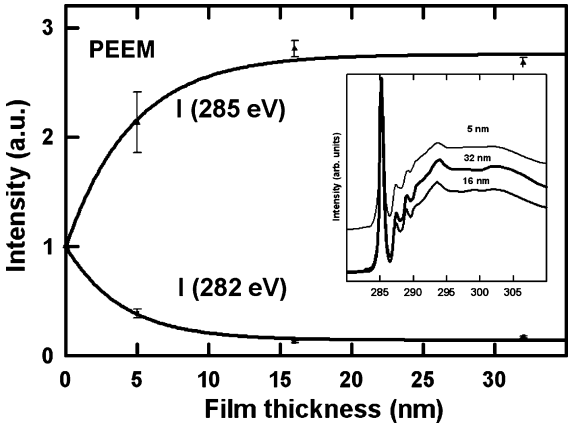

Fig. 1. X-PEEM signal intensity at 285 and 282 eV as a function of the thickness of a spun cast polystyrene (PS) film on a native oxide silicon substrate. The film thickness was determined from the height profile across a scratch in an AFM image. The exponential fits to the increase in the C 1s → π* signal and the decrease in the Si 2p continuum signal correspond to a sampling depth (1/e) of 4 nm. The inset plots the measured C 1s spectra. The large pre-edge signal seen for the 5 nm thin film is caused by electrons from the underlying Si substrate.

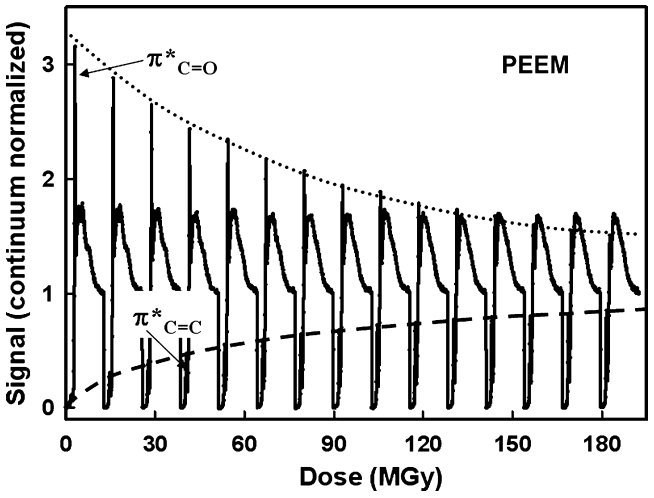

Fig. 2. Sequence of C 1s spectra of PMMA recorded by X-PEEM with a reduced flux on the same area. The integrated dose accrued during the 150 s it took to record each spectrum was 13 (± 1.3) MGy.

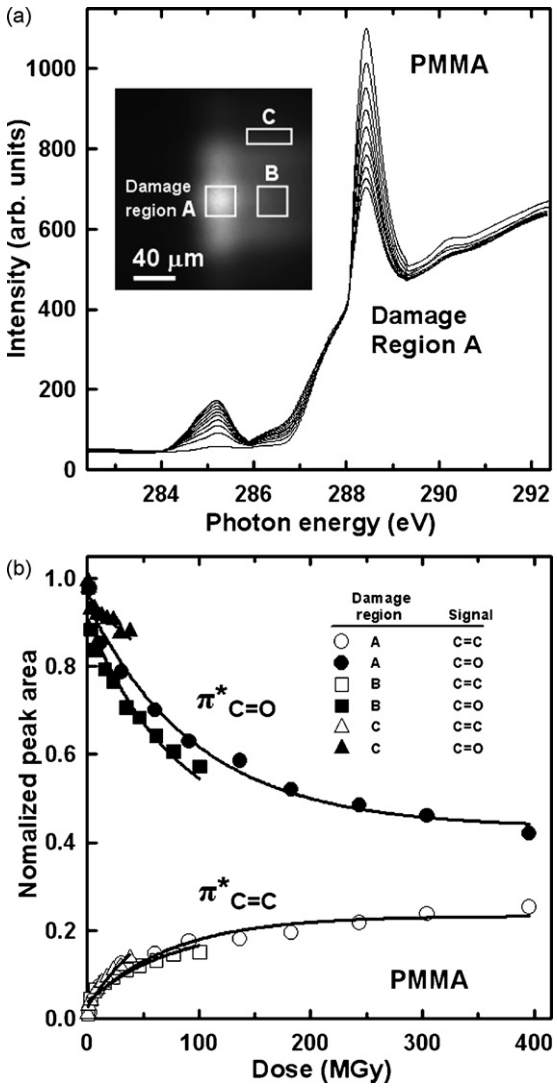

Fig. 3. (a) Sequence of C 1s spectra of PMMA recorded by X-PEEM in region A. The inset X-PEEM image indicates the three different illumination regions monitored for radiation damage. (b) Plots of the peak area of the C 1s → $\pi^*_{C=O}$(288.4 eV) and the C 1s → $\pi^*_{C=O}$(285.1 eV) transitions as a function of radiation dose for regions A, B and C.

have a range of radiation doses. Fig. 3a plots the sequence of spectra of region A, the highest dose area. Fig. 3b plots the normalized peak areas at 288.4 and 285.1 eV as a function of radiation dose for all three damage regions. The curves are fit to Eq. (3) from which a critical dose was determined. The damage saturation level from the data of region A was also used for analysis of the data of regions B and C. Due to mass loss and thus additional signal contributions from deeper layers (>10 nm) of the sample in X-PEEM, the damage saturated PMMA spectrum may still show some $\pi^*_{C=O}$ intensity. The saturation level for X-PEEM damage to PMMA is thus defined as that dose where there is no longer further change of the $\pi^*_{C=O}$ peak intensity. The critical dose from the data shown in Fig. 3, as well as from a repeat measurement at a different area of the sample conducted on a different date are summarized in Table 1. The critical dose for C=O loss or destruction was found to be 92 (14) MGy, while the critical dose for C=C generation was 71 (11) MGy. While the dose rate varies considerably in the different regions of the illumination, there is no obvious trend of critical dose with dose rate. The critical dose for C=O loss was always found to be higher than that for C=C growth, although the difference is within the uncertainties of the measurements as determined from the replicates. If there is a real difference, it could be due to the existence of different reaction pathways with different reaction rate for the two types of chemical change (see further discussion in Section 4).

Table 2 lists the critical doses for radiation damage of PMMA in X-PEEM, determined at the C 1s and O 1s edges through exposure at 280–320 and 525–565 eV, respectively. The radiation dose was obtained by integrating the incident flux spectrum through the entire exposure energy region, taking into account the optical density spectrum of PMMA for a 10 nm sampling depth and the exposure time at each energy point. The damage was monitored by measuring the spectral intensity change at four different photon energies (285.1, 288.4, 531.2 (O 1s (CO) → $\pi^*_{C=O}$) and 534 eV (O 1s (OCH_3) → $\pi^*_{C=O}$)). Plots of the signal change against dose were fit to Eq. (3) to find the critical doses. The results obtained from this method are summarized in Table 2. They are comparable to those reported in Table 1, even though the exposure protocol for the latter is rather different. Table 2 also compares our results to those measured by STXM from the literature [32,35,36]. The average value for the critical dose for decrease in the $\pi^*_{C=O}$ peak is similar to but larger than that reported elsewhere [35,36]. Zhang et al. [35] reported critical doses for soft X-ray damage of PMMA ranging from 11 to 69 MGy and suggested that the critical dose at 288.4 eV is much larger than that at 285.1 eV [35]. Our quantitative critical dose values (Tables 1 and 2) and the qualitative spectroscopic data (Fig. 2) strongly suggest that the rate of change of the signals at these two energies are quite similar, in disagreement with their observations.

3.3. PMMA – radiation damage in STXM

Fig. 4 presents results of a STXM measurement of radiation damage in PMMA. Fig. 4a is an optical density image of a uniform region of a PMMA film that was damaged in a 3 × 3 pattern of nine 600 nm × 600 nm (10 × 10 pixel) pads where each successive pad was subjected to a systematically increased dose rate by adjusting the dwell time per pixel between 12.5 and 500 ms. Fig. 4b plots the damage derived from the change in the optical density in the central 60% of each pad against the dose. Fig. 4c is the linearized version of that data fit to Eq. (3) to determine the critical dose. The critical dose for damage to PMMA with 300 eV incident photons, as measured by the decrease in the C 1s → $\pi^*_{C=O}$ peak intensity is summarized in Table 3, in comparison to literature

Table 1
Reproducibility of dose–damage data from X-PEEM measurements on PMMA with various dose rates

Sample	Exposure energy (eV)	Dose rate (MGy/s)	Critical dose (MGy)	
			C=C growth	C=O damage
60208-7 – region A	300	0.51	76 (11)	98 (15)
60208-7 – region B	300	0.13	74 (11)	79 (12)
60208-7 – region C	300	0.049	60 (9)	99 (15)
60211-3	300	0.098	74 (11)	91 (14)
Average	–	–	71 (11)	92 (14)

Table 2
Critical doses for radiation damage of PMMA, PS and Fg at C 1s, N 1s and O 1s edges as determined by X-PEEM

Material	Exposure energy (eV)	Dose rate (MGy/s)	Analysis energy (eV)	Critical dose (MGy)	
				X-PEEM	Literature (STXM)
PMMA	280–320	0.18	285.1	96 (14)	10.8[35]; [12.3[35a]]
			288.4	101 (15)	50[35], 69[36b]; [13.1[35a,c]]
	525–565	0.42	531	133 (20)	[18[32a,c]]
			534	143 (20)	–
PS	280–330	0.56	285.1	1200 (180)	–
Fg	280–320	0.20	285.1	540 (80)	–
			288.2	270 (40)	–
	390–450	0.28	397	300 (45)	–
			401	345 (52)	–
	525–565	0.46	531	300 (45)	–

[a] The PMMA film was annealed at 150 °C for 2 h.
[b] Converted from the reported value of 520 eV/nm^3 using 1 MGy = 6.242*ρ eV/nm^3, where ρ is the polymer density in g/cm^3.
[c] Note that the critical dose for PMMA films was found to be quite sensitive to annealing, with values measured at 288.4 eV changing from 50 for unannealed films to 13–15 MGy for films annealed at 150–200 °C [35]. Since we did not anneal our films for these studies, the relevant value to compare from Ref. [35] is 50 MGy.

values. The uncertainties cited are obtained from replicates. The derived critical dose of 67 ± 10 MGy for damage to PMMA measured at 288.45 eV is in good agreement with the values in the literature [35,36]. We note that the critical dose of 69 MGy reported in Ref. [36] (converted from 520 eV/nm^3) was cited as 14 MGy in Ref. [32]; probably the latter is the normalized carbonyl critical dose, which is computed from the critical dose by multiplying by the number of carbonyl groups, then dividing by the total number of carbon atoms in the monomer [36].

Zhang et al. [35] have shown that the critical dose for PMMA is sensitive to annealing, with values measured at 288.4 eV changing from 50 MGy for unannealed films to 13–15 MGy for films annealed at 150–200 C [35]. Our results are consistent with the critical dose reported by Zhang et al. [35] for the as-prepared PMMA films, without high temperature annealing. Further studies may be needed to clarify the effect of annealing on critical dose for radiation damage to PMMA. Apart from differences in sample preparation, critical doses may be significantly influenced by a number of other factors, including measurement environment [36], second order light, detector efficiency, damage data extraction errors, change of photon flux during damage, variation of sample thickness and definition of the saturation level, etc. Systematic errors associated with the first three factors can be minimized through use of a helium environment, use of a second order filter, and careful calibration of the detector efficiency, respectively. The remaining factors contribute much less to the total uncertainty although defining the damage saturation level is somewhat arbitrary, especially for cases where the extent of damage is low. We estimate the total uncertainty to be about 15% for our STXM damage studies. A similar magnitude of uncertainty was also estimated for the results of the X-PEEM damage studies although the contributing factors are different in the two techniques. For example, in X-PEEM the determination of irradiation area and volume gives rise to the largest uncertainties.

3.4. Dose–damage relationships for PMMA, PS and Fg in X-PEEM and STXM

Methods similar to those described for PMMA in the preceding sections were also applied to measurements of dose–damage relationships for polystyrene (PS) and fibrinogen (Fg), in both X-PEEM and STXM. Fig. 5 plots the normalized radiation damage as a function of dose for PMMA, PS and Fg as measured in X-PEEM. The derived critical doses for these species at different edges as monitored at a number of photon energies are summarized in Table 2. Fig. 5a plots PMMA dose–damage results measured at both C 1s and O 1s edges. The variation in the incident flux over the spectral region (C 1s: from 282 to 320 eV; O 1s: from 525 to 565 eV) was taken into account in deriving these results. The damage as a function of dose is similar for both edges. The critical doses for damage at the O 1s edge derived from these measurements are slightly larger than those at the C 1s edge. Beetz and Jacobsen [32] also found a somewhat higher critical dose for an annealed PMMA sample at the O 1s edge compared to the C 1s edge (18 versus 13 MGy). However, this difference is probably not outside the uncertainties in the measurement since there are large differences in the dose parameters at the two edges. Systematic errors in the absorption coefficient, the incident flux (I_0) and the detection efficiency (ε) may exist when two different edges are compared.

Fig. 5b presents the damage versus dose curve for polystyrene measured with X-PEEM at the C 1s edge. There is a lot of mobile hydrocarbon contaminant present in the STXM (mostly from stage and motor lubricants). If the radiation dose is large enough, the hydrocarbon contaminants are cracked and deposited on the sam-

Table 3
Critical doses for radiation damage of PMMA, PS and Fg as determined by STXM

Material	Exposure energy (eV)	Dose rate (MGy/s)	Analysis energy (eV)	Critical dose (MGy)	
				STXM	Literature (STXM)
PMMA	300	3.7×10^2	288.4	67 (10)	50[35], 69[36b]; [13.1[35a,c]]
PS	285.1	5.3×10^2[d]	285.1	1260 (190)	–
Fg	300	5.9×10^2	288.2	298 (45)	–

[a] The PMMA film was annealed at 150 °C for 2 h.
[b] Converted from the reported value of 520 eV/nm^3 using 1 MGy = 6.242*ρ eV/nm^3, where ρ is the polymer density in g/cm^3.
[c] Note that the critical dose for PMMA films was found to be quite sensitive to annealing, with values measured at 288.4 eV changing from 50 for unannealed films to 13–15 MGy for films annealed at 150–200 C [35]. Since we did not anneal our films for these studies, the relevant value to compare from Ref. [35] is 50 MGy.
[d] Average from the dose rate range of 5.7×10^2 to 4.9×10^2 MGy/s.

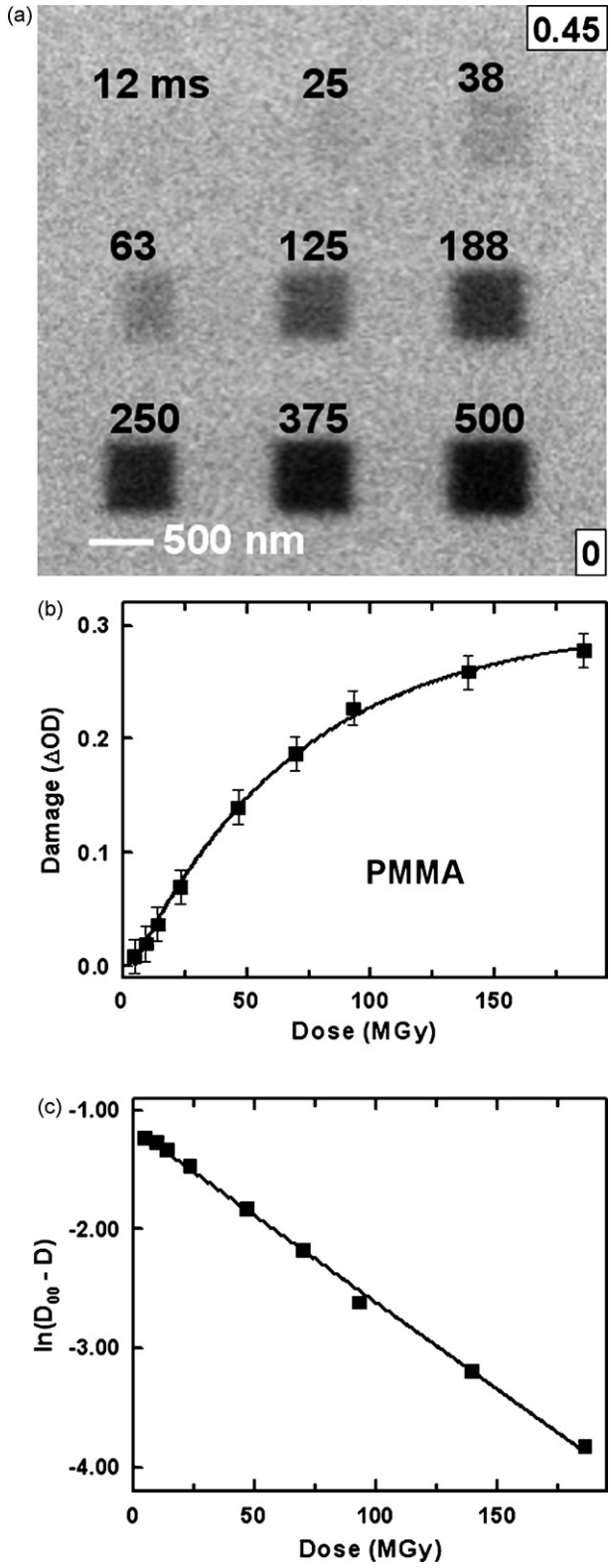

Fig. 4. STXM damage of PMMA. (a) Patterns created in an initially undamaged, free standing PMMA thin film by exposure at 300 eV (dose rate = 3.7×10^2 MGy/s) using a 10×10 pixel, 0.6×0.6 μm raster scan with the indicated per-pixel dwell times The image was recorded after the exposure at 288.45 eV using ~1/3rd the dose rate used to create the radiation damage. The numbers in the lower and upper left boxes are the optical density limits to the image gray scale. (b) Plot of damage (determined from the central 60% of each pad) versus dose. (c) Linearized plot of the data of (b) corresponding to the analysis (Eq. (3)) used to derive the critical dose.

ple surface, leading to an increase in the C 1s continuum signal. Initial dose–damage measurements on PS were negatively influenced by this effect. In order to avoid this problem in measuring the critical dose for PS, the exposure was performed at 285.1 eV where the absorbance of the hydrocarbon contaminants is low, the absorbance by PS is maximum, and thus the photo deposition rate is much less than the damage rate. When the exposure energy is 285.1 eV, carbon build-up did not occur, even at the highest radiation dose used. However, when irradiation was performed at 320, 300 and 390 eV there were large increases in the C 1s continuum signal at the doses needed to visibly damage PS. When PS is damaged at 285.1 eV in STXM, there is a significant decrease of the absorbance since breaking the phenyl rings is the main consequence of the radiation damage (see Section 4). In order to account for the changing absorbance, the dose was evaluated by integrating the optical density over the exposure time using the following equation:

$$S_{OD} = \frac{\int_0^t (y_0 + ce^{-bt})dt}{t} = \frac{y_0 t + (c/b)\ (1 - e^{-bt})}{t} \quad (4)$$

where S_{OD} is the integrated optical density up to time, t and y_0, c and b are fitting constants. The critical dose for chemical damage to PS is much larger than that for PMMA. This is as expected since it is much more difficult to break the stable phenyl group than to remove CO_2 from PMMA. The critical dose for PS derived from this measurement is 1200 (180) MGy.

Fig. 5c presents the damage versus dose curves for fibrinogen (Fg) as monitored at five energies around the C 1s, N 1s and O 1s edges. The signals at 288.2 eV (C 1s → $\pi^*_{C=O}$) and 285.1 eV (C 1s → $\pi^*_{C=C}$) show complicated non-exponential signals. This could be due to the interplay of a number of different damage processes, such as damage and rearrangement of amide groups, damage of radiation sensitive R-groups, etc. which could have quite different characteristic doses such that multiple exponential are required to fit the dose–damage curve. In these cases, the curve fitting was performed on that sub-set of the data points which best represents a single exponential change in the intensities of the C 1s → $\pi^*_{C=O}$ and C 1s → $\pi^*_{C=C}$ peaks. As with PMMA, the critical doses for damage of Fg at different edges are comparable except for the change in the C 1s → $\pi^*_{C=C}$ signal. The derived critical doses are intermediate between those for PS and PMMA.

Fig. 6 shows the damage versus dose curves for PMMA, PS and Fg derived from STXM measurements at the C 1s edge. The samples were irradiated at 300, 285.1 and 300 eV, respectively, while the damage was evaluated from changes in image contrast at 288.45 (C 1s → $\pi^*_{C=O}$ transition) for PMMA, 285.1 (C 1s → $\pi^*_{C=C}$ transition) for PS, and 288.2 eV (C 1s → $\pi^*_{C=O}$ amide transition) for fibrinogen. In Fig. 6 the damage signals for the three molecules are presented after normalization to the saturation level for ease of comparison. The critical doses derived from fitting these curves are listed in Table 3, i.e. the critical doses for PMMA, PS and Fg in STXM are 67 (10), 1260 (190) and 298 (45) MGy, respectively. The relative ordering of the critical doses is the same as found in X-PEEM. PMMA is by far the most sensitive of the three materials, with Fg more sensitive (lower critical dose) than PS.

While the trends in relative damage rates are similar for the two different microscopies, there are still some differences between the critical doses derived from the two techniques. This could be related to the different sample environments, combined with the very different doses needed to damage each polymer. The sample is in a very clean UHV environment in X-PEEM whereas the sample is in He at 1/3rd of atmospheric pressure in the STXM. This environmental change could also affect aspects of the secondary damage process such as electron transport. It is also possible there are

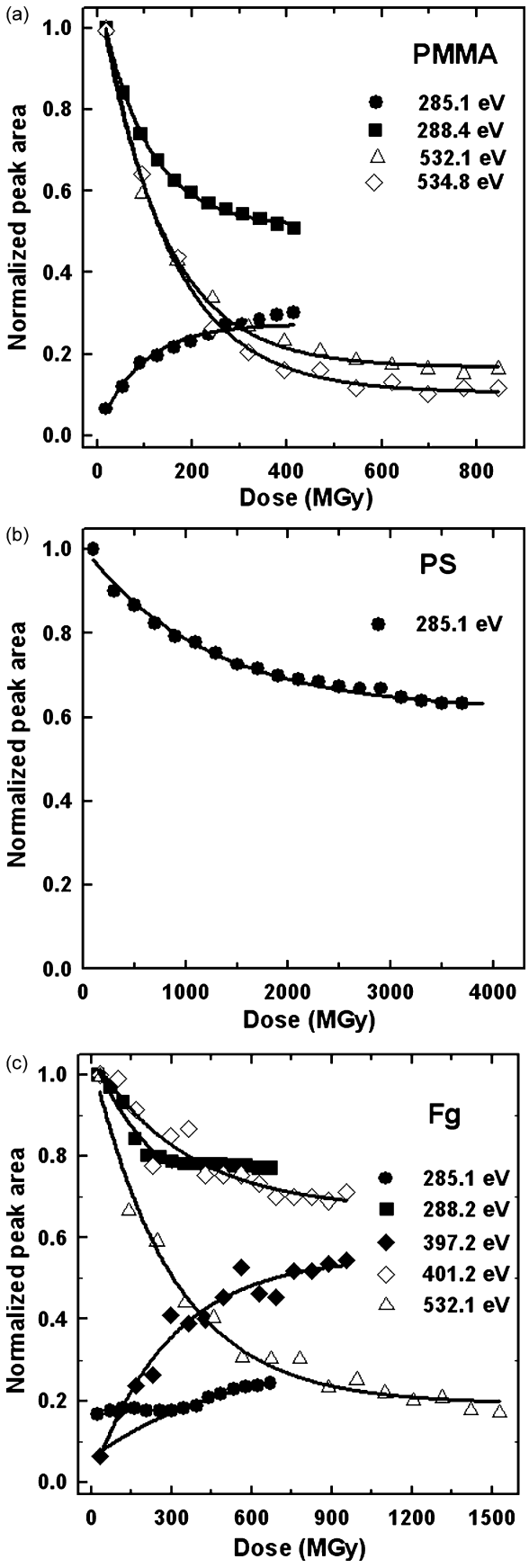

Fig. 5. Damage versus dose curves for (top) PMMA, (middle) PS and (lower) Fg derived from X-PEEM spectral measurements at the C 1s, N 1s (Fg) and O 1s edges.

undetected systematic errors, such as detection efficiency (ε) or calibration of the incident flux (I_0). Finally there are large differences in the dose rate—X-PEEM dose rates (100–500 kGy/s) are three orders of magnitude smaller than those of STXM (300–600 MGy/s) and it is possible that the critical dose changes as a function of dose rate.

The relative damage rates for these three materials are PMMA > Fg > PS, or conversely, the critical dose is the smallest for PMMA and the largest for PS. These measurements monitor the fast chemical change and ignore slower processes such as mass loss. Zhang et al. [35] and Coffey et al.[36] considered both processes, and showed that mass loss occurs at a much slower rate. Since the motivation for this study is to determine critical doses to guide chemical analysis (i.e. doses below that which significantly modifies the NEXAFS spectrum), we consider our operational definition of the critical dose as the appropriate one to use. Note that mass loss has little effect in these X-PEEM measurements since the sample is ~40 nm thick, whereas the sampling depth is less than 10 nm and thus there is always material (albeit damaged) from deeper in the sample even when mass loss is occurring. The mass loss is readily detected in STXM since it samples the full thickness of the film.

4. Chemical changes from radiation damage as probed by NEXAFS

Fig. 7 compares the C 1s spectra of undamaged and heavily damaged PMMA, PS and Fg from STXM. The radiation damage induced changes in the NEXAFS spectra are the same in STXM and X-PEEM and thus the same structural changes are occurring. In PMMA the most prominent change is the decrease in the 288.45 eV peak corresponding to loss of C 1s → $\pi^*_{C=O}$ transitions as $COOCH_3$ or CO_2 is removed. At the same time, signal grows at 285.1 eV peak, the C 1s(C═C) → $\pi^*_{C=C}$ transition, associated with re-organization and introduction of an unsaturated C═C bond. A third aspect is the disappearance of a weak peak at 290 eV and the C 1s → $\sigma^*_{C=O}$ signal at 296 eV.

Radiation damage in PS takes the form of loss of intensity at the 285.1 eV C 1s(C═C) → $\pi^*_{C=C}$ transition associated with damage to the phenyl ring, and a simultaneous increase in signal at 284.5 eV, attributed to dehydrogenation of the saturated backbone chain. The destruction of the aromatic rings is also indicated by loss of the C 1s → $2\pi^*$ transition (289 eV) and the double peaked C 1s → $\sigma^*_{C=C}$ continuum signals (293, 303 eV), both of which are characteristic of phenyl rings [51]. The C 1s continuum intensity stays constant with dose indicating that there is negligible mass loss during radiation damage of PS, a result also reported by Coffey et al. [36]. A very weak signal grows at 286.5 eV. It is assigned to C 1s(C═O) → $\pi^*_{C=O}$ transitions in carbonyls probably formed from oxidation of PS, since residual oxygen and oxygen-containing contaminants may be present during STXM measurements.

Radiation damage of Fg is dominated by loss of the C 1s → $\pi^*_{C=O}$ transition at 288.2 eV. In this case, CO_2 is not likely to be a dominant radiation product since there is no oxygen atom adjacent to the carbonyl. C═N double bond formation and elimination of water are more likely. The formation of C═N bonds is consistent with the growth of signals at 398–399 eV (N 1s → $\pi^*_{C=N}$ transitions, see below) and at 287 eV (C 1s → $\pi^*_{C=N}$ transitions) [52]. There is relatively little, if any, increase in signal at 285 eV consistent with the presence of relatively few saturated CH–CH linkages in pro-

See Table 2 for details of the exposure energies and average dose rates used. The damage signal corresponds to the peak area as monitored at the photon energies listed in Table 2. The solid curves are fits to exponentials from which the critical doses were derived.

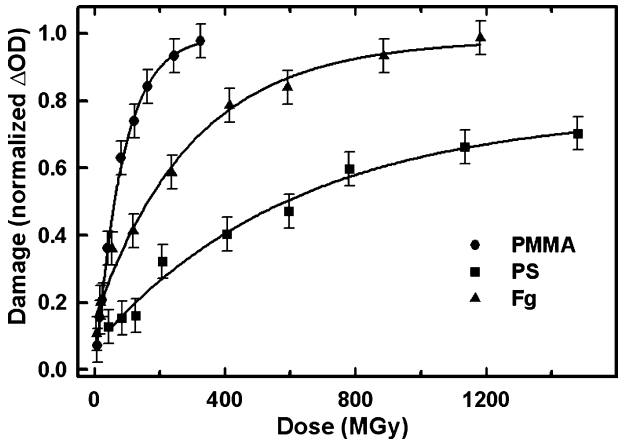

Fig. 6. Damage versus dose curves for PMMA, PS and Fg derived from STXM damage pattern spectral measurements at the C 1s edge. The exposure energy and dose rates are listed in Table 3. The damage signal, which is the change in optical density monitored at the photon energies listed in Table 3, tracks the amount of damaged product and thus integrates over possible different damage rates for different reactions. To allow comparison the damage signals are normalized to a value of 1 at the signals for infinite dose (see text).

teins which are the structures that are most susceptible to radiation induced dehydrogenation.

Fig. 8 compares the N 1s spectra of damaged and undamaged Fg and the O 1s spectra of damaged and undamaged Fg and PMMA. The signature of radiation damaged proteins at the N 1s edge is a decrease in intensity at 401.2 eV, the N 1s $\rightarrow \pi^*_{C=O}$ amide transition [53], and the creation of two sharp signals at 398 and 399 eV. The latter peaks are attributed to formation of C=N bonds with different local environments. Mass loss during radiation damage of Fg is also evident since the N 1s $\rightarrow \sigma^*$ transition at 403 eV and the N 1s continuum intensities decrease significantly. This probably involves evolution of NH_3. At the O 1s edge the O 1s $\rightarrow \pi^*_{C=O}$ transition at 532.1 eV is selectively lost, and there is large loss of oxygen atoms, as indicated by the decrease in the O 1s continuum signal. The damage observed at the O 1s edge for PMMA parallels that seen in the C 1s edge. In particular, the O 1s(C=O) $\rightarrow \pi^*_{C=O}$ transition decreases in intensity, as does the O 1s(OCH_3) $\rightarrow \pi^*_{C=O}$ transition at 534.8 eV. Mass loss in PMMA is much more visible in the O 1s than the C 1s edge since all of the oxygen atoms in a given repeat unit are lost when CO_2 is evolved.

Fig. 9 presents some possible reactions involved in the radiation damage of these three materials. These suggestions are based on the spectral changes observed. Fig. 9a presents some possible pathways for radiation damage of PMMA. The first damage pathway involves the loss of the ester side group and 1,2 H-migration, leading to formation of C=C bonds in the main chain of the polymer. The second pathway also involves the loss of ester group and then the main chain is cleaved to form an end group with a C=C bond. This main-chain scission was proposed by David et al. [54]. These two possible pathways would result in a decrease in the intensity of the 288.4, 532.1 and 534.8 eV peaks, and the creation of signal at 285.1 eV. The third possible pathway involves decarboxylation, which would cause decreased intensity of the 288.4, 532.1 and 534.8 eV peaks, the major spectral changes. Since there are different pathways contributing to two different spectral changes in the C 1s spectrum, it is possible that the dose–damage rate derived from spectral change at 288.4 and 285.1 eV will differ. The critical dose for C=O loss is somewhat higher than that for C=C growth as derived by X-PEEM measurements.

Fig. 9b presents three possible damage pathways for PS. The first one involves dehydrogenation of the C–C backbone. Typically the

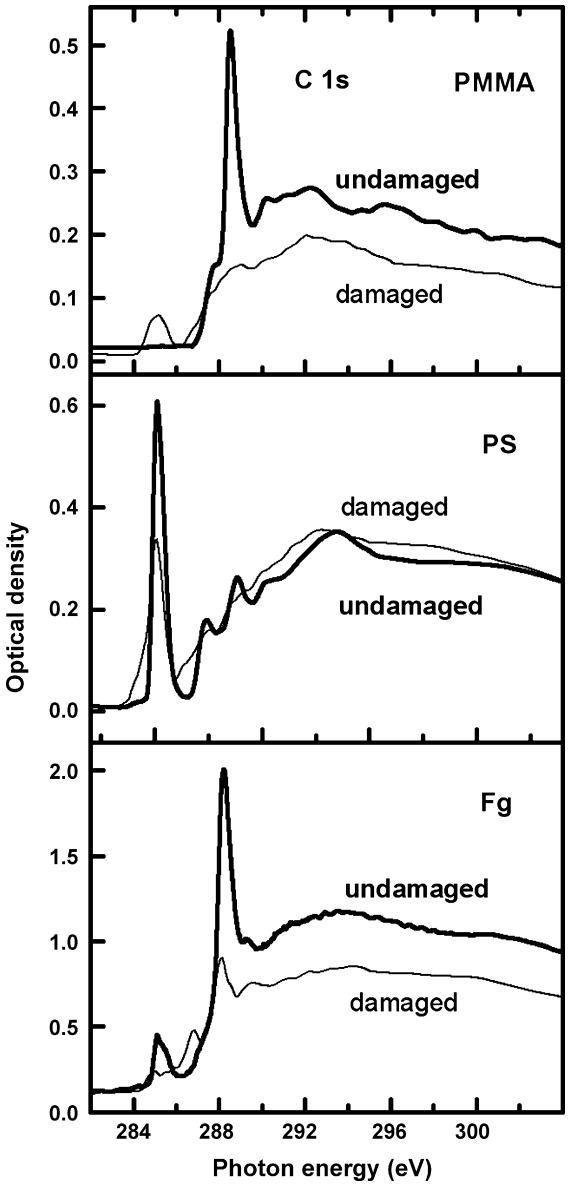

Fig. 7. Changes with radiation damage in the C 1s spectra recorded by STXM for PMMA, PS and Fg. The thicker line corresponds to the undamaged material, while the thinner line corresponds to a heavily radiation damaged sample. Mass loss is indicated by changes in the continuum intensity above 296 eV.

C 1s $\rightarrow \pi^*_{C=C}$ transition for backbone unsaturation comes at lower energy than the $\pi^*_{C=C}$ in aromatic rings. Thus, the appearance of the low energy shoulder at 284.5 eV may be explained this way. The second pathway represents damage to the rings where one or more of the double bonds are saturated by hydrogen generated from the first pathway, or, more likely, by abstraction of H from the backbone of adjacent PS chains or phenyl rings. Breakage of the aromatic ring structure is a surprisingly important reaction, which leads to the observed decrease in the main $1\pi^*$ peak and creation of lower energy $\pi^*_{C=C}$ signals. Mass loss could occur by elimination of hydrocarbon fragments, as represented by the third pathway. However, this is a low probability process since there is negligible change in the C 1s continuum intensity.

Fig. 9c shows proposed reactions for radiation damage to the fibrinogen protein. While some loss of the 288.2 eV $\pi^*_{C=O}$ feature is undoubtedly associated with loss of CO_2 from the acid terminal end, this is a very small portion of the total protein. Thus, a dam-

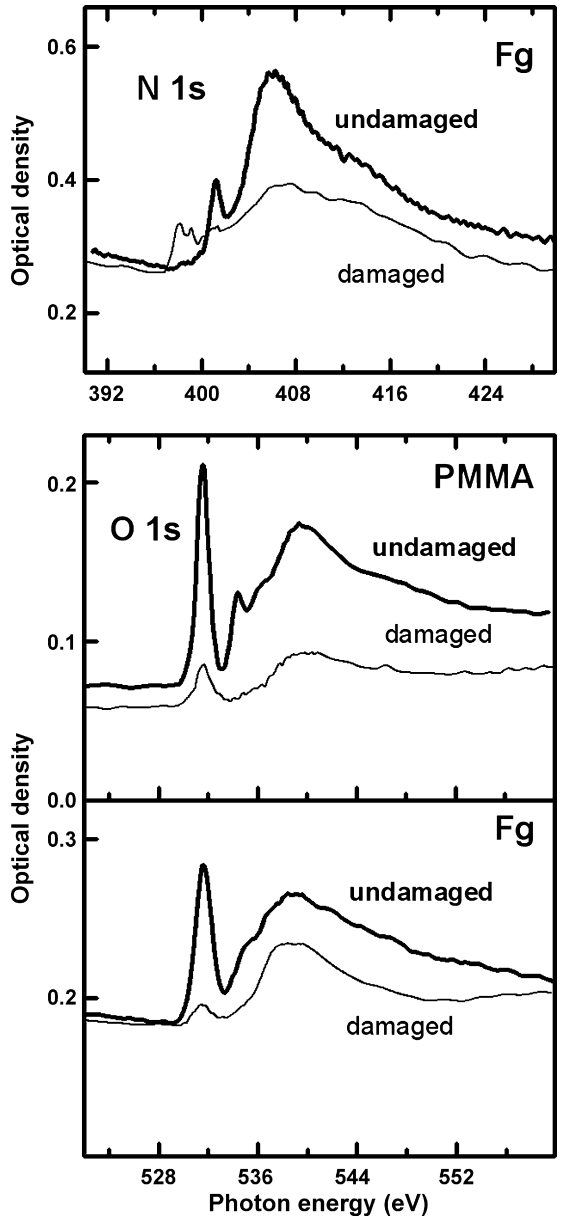

Fig. 8. Changes with radiation damage in the N 1s spectra of Fg recorded by STXM, and in the O1s spectra of PMMA and Fg by STXM. The thicker line corresponds to the undamaged material, while the thinner line corresponds to a heavily radiation damaged sample. Mass loss is indicated by changes in the continuum intensities.

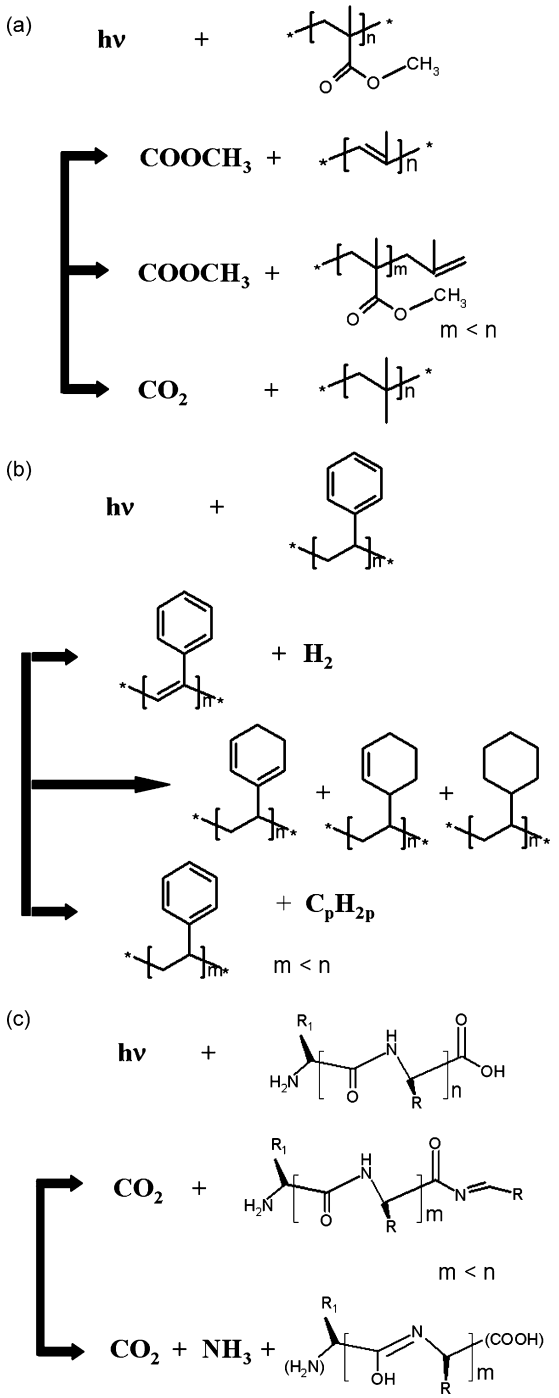

Fig. 9. Proposed reactions for radiation damage of (a) PMMA; (b) PS; and (c) Fg.

age reaction, such as that shown in Fig. 9c, which leads to loss of the C=O bond and formation of a C=N bond is required, and would be consistent with the formation of C 1s → $\pi^*_{C=N}$ and N 1s → $\pi^*_{C=N}$ excitation signals. More than one structure containing C=N bonds can be envisaged, and this is suggested by the presence of fine structure in the 399–400 eV region of the spectrum of damaged fibrinogen. Note that both the N 1s and O 1s continuum intensities change significantly, indicating large mass loss. This suggests contributions from a reaction that involves degradation of the protein and generation of small molecules, such as CO_2, NH_3 and amino acids. The full set of radiation damage reactions in proteins is very complicated and probably impossible to figure out in detail using only NEXAFS spectroscopy. For example, a number of studies of the radiation damage chemistry of individual amino acids [34,55–57] have shown that the decomposition induced by soft X-rays follows a number of pathways, including dehydration, decarboxylation, decarbonylation, deamination and desulfurization, accompanied by desorption of H_2, H_2O, CO_2, CO, NH_3 and H_2S with rates depending on the specific amino acid. In general, while these various reactions are consistent with the observed spectral changes, there are many other possible structures that could also give rise to the changes. Given the probably very reactive character of the radicals and ions produced in X-ray ionization and subsequent secondary events, a wide variety of reaction products may be formed.

Although radiation damage to polymers and other materials initiated by soft X-rays is a complicated process with many contributing factors, it can be generally characterized by two phases, i.e. the initial photoabsorption and femtosecond scale electronic

decay at the site of the X-ray absorption (a single atom), and subsequent secondary processes [58] on a longer time scale (picosecond to seconds) which produce secondary electrons, free radicals and ions. These particles extend the range of the damage [59] and are responsible for creating a cascade of damage to the irradiated material. The transport range of electrons is limited to a few tens of nanometers at most due to their strong interactions in condensed media. It is probably energetic radicals or ions that are responsible for the longer range effects since they are much more damaging and there is the possibility of chain processes. Reaction of these radicals and ions with nearby molecules can create new radicals/ions thereby setting up a chain reaction which can transfer the damage to regions far (~100 nm) from the initial absorption site. This process can be viewed as radical or ion initiated chain depolymerization or fragmentation. Another factor that might contribute is localized heating and associated thermal damage. However, this has been shown to be a minor effect [59].

The soft X-ray radiation damage studies of this work are not only essential to X-ray spectromicroscopy analysis of radiation sensitive materials such as polymers and biological samples, but also may have potential applications in X-ray lithography and other types of nanofabrication involving surface or bulk chemical modification by soft X-rays. We have demonstrated a novel method with STXM that adds chemical selectivity to lithography. Specifically, the X-ray absorption in a bilayer [59] or trilayer [60] polymer system is used to pattern with chemical selectivity through radiation damage to each polymer layer without affecting other layers. The other feature of this method is the direct-write capability, which is controlled by a pattern generation program, incorporated into the microscope control and data acquisition software. Input files for pattern generation consist of lists of (x, y, t, E) values for each pixel. This approach was used to make the 3×3 patterns of pads covering a range of doses which were used for quantitative dose–damage analysis in this work. This has made radiation damage studies more efficient with STXM.

5. Recommended procedures for X-ray microscopy studies of radiation sensitive samples

1. Identify the more damage-sensitive chemical components in the system under study. Usually inorganic materials are more robust under radiation than organic materials. Among the latter, saturated compounds tend to be more radiation sensitive than unsaturated compounds. Species with C–O single and double bonds are also quite sensitive.
2. Use the least damaging sample environment possible (in the STXM, this is either a low vacuum ($P \sim 0.1$ torr), or 1/3 atm pressure of He).
3. When it is clear radiation damage will be critical, measure the critical dose using procedures similar to this work, and use that as a guideline for measurement protocols. Typically we find 20% of the critical dose as a practical limit to acceptable levels of damage.
4. Use the lowest dose possible to survey the sample for interesting sample regions.
5. Adjust the dose on the sample through slits or dwell time to keep the dose below acceptable limits. Within that limit, adjust the experimental conditions to provide best possible statistics, spatial and spectral resolution.
6. In STXM, image sequences [49] give the best results, with line scan spectra often adequate but point spectra in fully focused mode rarely being appropriate. If the full spatial resolution is not needed, a slight defocus of the STXM beam can be very helpful at avoiding radiation damage.
7. After each analytically critical measurement, check if radiation damage occurs by recording an image at a damage-sensitive energy.

6. Summary

Quantitative radiation damage rates of poly(methylmethacrylate), polystyrene and fibrinogen have been measured in an X-ray photoemission electron microscope (X-PEEM) and in a scanning transmission X-ray microscope (STXM). Similar critical dose values were obtained for both microscopes. The critical doses for PMMA damage (the only species in this study for which literature data is available) are in good agreement with literature measurements of unannealed PMMA [35,36]. The order of sensitivity to X-ray radiation is PMMA > Fg > PS. The spectral changes in the C 1s, N 1s and O 1s regions have been used to deduce possible reactions involved in the damage chemistry.

Acknowledgements

This research is supported by NSERC (Canada) and the Canada Research Chair Program. Cynthia Morin acknowledges the support of an ALS graduate fellowship during which time much of this work was performed. We thank X. Zhang and T. Araki for assistance with the measurements. Construction and operation of the STXM 5.3.2 microscope is supported by NSF DMR-9975694, DOE DE-FG02-98ER45737, Dow Chemical, NSERC and the Canadian Foundation for Innovation. We thank David Kilcoyne, the 5.3.2 beamline scientist for his contributions to developing and maintaining the instrument. The Advanced Light Source is supported by the Director, Office of Energy Research, Office of Basic Energy Sciences, Materials Sciences Division of the U.S. Department of Energy, under Contract No. DE-AC03-76SF00098.

Appendix A. Supplementary data

Supplementary data associated with this article can be found, in the online version, at doi:10.1016/j.elspec.2008.01.002.

References

[1] C.L. Greenstock, Med. Hypotheses 41 (1993) 473.
[2] E.S. Kempner, J. Pharm. Sci. 90 (2001) 1637.
[3] A. Gonzalez, A.W. Thompson, C. Nave, Rev. Sci. Instrum. 63 (1992) 1177.
[4] J.R. Srour, C.J. Marshall, P.W. Marshall, IEEE Trans. Nucl. Sci. 50 (2003) 653.
[5] Radiation Effects on Polymers, in: R.L. Clough, S.W. Shalaby (Eds.), ACS Symposium Series 475, 1991;
Irradiation of Polymers: Fundamentals and Technological Applications, in: R.L. Clough, S.W. Shalaby (Eds.), ACS Symposium Series 620, 1996.
[6] B.P. Tonner, G.R. Harp, S.F. Koranda, J. Zhang, Rev. Sci. Instrum. 63 (1992) 564.
[7] G. De Stasio, M. Capozi, G.F. Lorusso, P.A. Baudat, T.C. Droubay, P. Perfetti, G. Margaritondo, B.P. Tonner, Rev. Sci. Instrum. 69 (1998) 2062.
[8] S. Anders, H.A. Padmore, R.M. Duarte, T. Renner, T. Stammler, A. Scholl, M.R. Scheinfein, J. Stöhr, L. Séve, B. Sinkovic, Rev. Sci. Instrum. 70 (1999) 3973.
[9] E. Bauer, J. Electron Spectrosc. Relat. Phenom. 114–116 (2001) 975.
[10] J. Kirz, H. Rarback, Rev. Sci. Instrum. 56 (1985) 1.
[11] H. Rarback, D. Shu, S.C. Feng, H. Ade, J. Kirz, I. McNulty, D.P. Kern, T.H.P. Chang, Y. Vladimirsky, N. Iskander, D. Attwood, K. McQuaid, S. Rothman, Rev. Sci. Instrum. 59 (1988) 52.
[12] T. Warwick, K. Franck, J.B. Kortright, G. Meigs, M. Moronne, S. Myneni, E. Rotenberg, S. Seal, W.F. Steele, H. Ade, A. Garcia, S. Cerasari, J. Denlinger, S. Hayakawa, A.P. Hitchcock, T. Tyliszczak, J. Kikuma, E.G. Rightor, H.-J. Shin, B.P. Tonner, Rev. Sci. Instrum. 69 (1998) 2964.
[13] H. Ade, in: J.A.R. Samson, D.L. Ederer (Eds.), Experimental Methods in the Physical Sciences, vol. 32, Academic Press, New York, 1998, p. 225.
[14] H. Ade, S.G. Urquhart, in: T.K. Sham (Ed.), Chemical Applications of Synchrotron Radiation, World Scientific Publishing, Singapore, 2002, p. 285.
[15] A.L.D. Kilcoyne, T. Tyliszczak, W.F. Steele, S. Fakra, P. Hitchcock, K. Franck, E. Anderson, B. Harteneck, E.G. Rightor, G.E. Mitchell, A.P. Hitchcock, L. Yang, T. Warwick, H. Ade, J. Synchrotron Radiat. 10 (2003) 125.
[16] J.R. Lawrence, G.D.W. Swerhone, G.G. Leppard, T. Araki, X. Zhang, M.M. West, A.P. Hitchcock, Appl. Environ. Microbiol. 69 (2003) 5543.

[17] I.N. Koprinarov, A.P. Hitchcock, C.T. McCrory, R.F. Childs, J. Phys. Chem. B 106 (2002) 5358.
[18] I.N. Koprinarov, A.P. Hitchcock, W.H. Li, Y.M. Heng, H.D.H. Stöver, Macromolec. 34 (2001) 4424.
[19] T. Araki, A.P. Hitchcock, F. Shen, P. Chang, M. Wang, R.F. Childs, J. Biomater. Sci. Polym. Ed. 16 (2005) 611.
[20] C. Morin, H. Ikeura-Sekiguchi, T. Tyliszczak, R. Cornelius, J.L. Brash, A.P. Hitchcock, A. Scholl, F. Nolting, G. Appel, A.D. Winesett, K. Kaznacheyev, H. Ade, J. Electron Spectrosc. Relat. Phenom. 121 (2001) 203.
[21] A.P. Hitchcock, C. Morin, Y.M. Heng, R.M. Cornelius, J.L. Brash, J. Biomater. Sci. Polym. Ed. 13 (2002) 919.
[22] C. Morin, A.P. Hitchcock, R.M. Cornelius, J.L. Brash, S.G. Urquhart, A. Scholl, A. Doran, J. Electron Spectrosc. Relat. Phenom. 137–140 (2004) 785.
[23] L. Li, A.P. Hitchcock, N. Robar, R. Cornelius, J.L. Brash, A. Scholl, A. Doran, J. Phys. Chem. B 110 (2006) 16763.
[24] J. Kirz, C. Jacobsen, M. Howells, Q. Rev. Biophys. 28 (1995) 33.
[25] J. Maser, A. Osanna, Y. Wang, C. Jacobsen, J. Kirz, S. Spector, B. Winn, D. Tennant, J. Microsc. 197 (2000) 68.
[26] Y. Wang, C. Jacobsen, J. Maser, A. Osanna, J. Microsc. 197 (2000) 80.
[27] J.A. Brandes, C. Lee, S. Wakeham, M. Peterson, C. Jacobsen, S. Wirick, G. Cody, Mar. Chem. 92 (2004) 107.
[28] M.G. Anderson, T. Haraszti, G.E. Petersen, S. Wirick, C. Jacobsen, S.W.M. John, M. Grunze, Micron 37 (2006) 689.
[29] O. Dhez, H. Ade, S.G. Urquhart, J. Electron Spectrosc. Relat. Phenom. 128 (2003) 85.
[30] A. Schoell, Y. Zou, D. Huebner, S.G. Urquhart, T. Schmidt, R. Fink, E. Umbach, J. Chem. Phys. 123 (2005) 044509.
[31] G. Schneider, Ultramicroscopy 75 (1998) 85.
[32] T. Beetz, C. Jacobsen, J. Synchrotron Radiat. 10 (2002) 280.
[33] E.G. Rightor, A.P. Hitchcock, H. Ade, R.D. Leapman, S.G. Urquhart, A.P. Smith, G. Mitchell, D. Fischer, H.J. Shin, T. Warwick, J. Phys. Chem. B 101 (1997) 1950.
[34] Y. Zubavichus, O. Fuchs, L. Weinhardt, C. Heske, E. Umbach, J.D. Denlinger, M. Grunze, Radiat. Res. 161 (2004) 346.
[35] X. Zhang, C. Jacobsen, S. Lindaas, S. Williams, J. Vac. Sci. Technol. B 13 (1995) 1477.
[36] T. Coffey, S.G. Urquhart, H. Ade, J. Electron Spectrosc. Relat. Phenom. 122 (2002) 65.
[37] D. Veseley, D. Finch, in: G.J. Tatlock (Ed.), Electron Microscopy and Analysis 1985, Hilger, Bristol, 1985, p. 7.
[38] K. Dawes, L.C. Glover, in: J.E. Mark (Ed.), Effects of Electron Beam and γ-Radiation on Polymeric Materials, Physical Properties of Polymers Handbook, AIP Press, Woodbury, NY, 1996.
[39] L.W. Hobbs, in: J.J. Hren, J.I. Goldstein, D.C. Joy (Eds.), Introduction to Analytical Electron Microscopy, Plenum Press, New York, 1987, p. 399.
[40] L.C. Sawyer, D.T. Grubb, Polymer Microscopy, Chapman and Hill, New York, 1987.
[41] T.-Y. Teng, K. Moffat, J. Synchrotron Radiat. 7 (2000) 313.
[42] G. Beamson, D. Briggs, High Resolution XPS of Organic Polymers, Wiley, New York, 1992.
[43] Silson Ltd. JBJ Business Park, Northampton Road, Blisworth, Northampton, UK, NN7 3DW.
[44] R. Korde, C. Prince, D. Cunningham, R.E. Vest, E. Gullikson, Metrologia, 40 (2003) S145. Calibrated silicon photodiodes were obtained from International Radiation Detectors, 2527 West 237th Street Unit A, Torrance, CA 90505–5243.
[45] T. Warwick, H. Ade, D. Kilcoyne, M. Kritscher, T. Tyliszczak, S. Fakra, A. Hitchcock, P. Hitchcock, H. Padmore, J. Synchrotron Radiat. 9 (2002) 254.
[46] Zone plate provided by the Centre for X-ray Optics, LBNL.
[47] C. Jacobsen, S. Wirick, G. Flynn, C. Zimba, J. Microsc. 197 (2000) 173.
[48] B.L. Henke, E.M. Gullikson, J.C. Davis, At. Data Nucl. Data Tables 54 (1993) 181.
[49] M. Zharnikov, S. Frey, K. Heister, M. Grunze, J. Electron Spectrosc. Relat. Phenom. 124 (2002) 15.
[50] B.H. Frazer, B. Gilbert, B.R. Sonderegger, G. De Stasio, Surf. Sci. 537 (2003) 161.
[51] J.A. Horsley, J. Stöhr, A.P. Hitchcock, D.C. Newbury, A.L. Johnson, F. Sette, J. Chem. Phys. 83 (1985) 6099.
[52] E. Apen, A.P. Hitchcock, J.L. Gland, J. Phys. Chem. 97 (1993) 6859.
[53] G. Cooper, M. Gordon, D. Tulumello, C.C. Turci, K. Kaznatcheev, A.P. Hitchcock, J. Electron Spectrosc. Relat. Phenom. 137–140 (2004) 795.
[54] C. David, D. Fuld, G. Geuskens, Makromol. Chem. 139 (1970) 269;
C. David, D. Fuld, G. Geuskens, Makromol. Chem 160 (1972) 135;
C. David, D. Fuld, G. Geuskens, Makromol. Chem. 160 (1972) 347.
[55] M.J. Boack, Y. Zhou, S.D. Worley, J. Chem. Phys. 100 (1994) 8392.
[56] Y. Zubavichus, M. Zharnikov, A. Shaporenko, O. Fuchs, L. Weinhardt, C. Heske, E. Umbach, J.D. Denlinger, M. Grunze, J. Phys. Chem. A 108 (2004) 4557.
[57] E. Sagstuen, A. Sanderud, E.O. Hole, Radiat. Res. 162 (2004) 112.
[58] J. Cazaux, J. Microsc. 188 (1997) 106.
[59] J. Wang, H.D.H. Stöver, A.P. Hitchcock, T. Tyliszczak, J. Synchrotron Radiat. 14 (2007) 181.
[60] J. Wang, H.D.H. Stöver, A.P. Hitchcock, J. Phys. Chem. C 111 (2007) 16330.